

UC Santa Barbara

UC Santa Barbara Previously Published Works

Title

Modeling crosshatch surface morphology in growing mismatched layers. Part II: Periodic boundary conditions and dislocation groups

Permalink

<https://escholarship.org/uc/item/9qr796wv>

Journal

Journal of Applied Physics, 95(11)

ISSN

0021-8979

Authors

Andrews, A M
LeSar, R
Kerner, M A
et al.

Publication Date

2004-06-01

Peer reviewed

Modeling crosshatch surface morphology in growing mismatched layers. Part II: Periodic boundary conditions and dislocation groups

A. M. Andrews, R. LeSar, M. A. Kerner, and J. S. Speck^{a)}
Materials Department, University of California, Santa Barbara, California 93106

A. E. Romanov
Ioffe Physico-Technical Institute, Russian Academy of Sciences, Polytechnicheskaya 26, RU-194021,
St. Petersburg, Russia

A. L. Kolesnikova
Institute for Problems of Mechanical Engineering, Russian Academy of Sciences, Bolshoj 61, Vas. Ostrov,
RU-199178, St. Petersburg, Russia

M. Bobeth and W. Pompe
Technical University Dresden, Hallwachsstrasse 3, 01062, Dresden, Germany

(Received 10 December 2003; accepted 25 February 2004)

We present further developments and understanding of the commonly observed crosshatch surface morphology in strain-relaxed heteroepitaxial films. We have previously proposed that the crosshatch morphology is directly related with strain relaxation via threading dislocation glide which results in both surface step and misfit dislocation (MD) formation [see Andrews *et al.*, *J. Appl. Phys.* **91**, 1933 (2002)—now referred to as Part I]. In this article, we have used solutions for the stress fields and displacement fields for periodic MD arrays which include the effects of the free surface. These solutions avoid truncation errors associated with finite dislocation arrays that were used in Part I. We have calculated the surface height profile for relaxed films where the misfit dislocations were introduced randomly or the misfit dislocations were placed in groups with alternating sign of the normal component of their Burgers vector. We have calculated the surface height profiles where the slip step remains at the surface [“slip step only” (SSO)] and where the slip step is eliminated [“slip step eliminated” (SSE)] due to annihilation of opposite sense steps, such as could happen during growth or lateral mass transport. For relaxed films, we find that the surface height undulations, characteristic of crosshatch, increase with increasing film thickness for the SSO case, whereas the surface becomes flatter for the SSE case. Experiments on relaxed $\text{In}_{0.25}\text{Ga}_{0.75}\text{As}$ films on (001) GaAs show that the surface height undulations in the [110] direction increase with increasing film thickness. Thus, we conclude that with increasing film thickness the crosshatch in the slow diffusion [110] direction is best described by the SSO case. © 2004 American Institute of Physics.
[DOI: 10.1063/1.1707208]

I. INTRODUCTION

Crosshatch is a common surface morphology that is observed after plastic strain relaxation in the heteroepitaxy of mismatched layers which grow in a two-dimensional mode (either layer-by-layer or step-flow growth). Crosshatch surfaces show a characteristic undulating morphology with hills and valleys parallel to the intersection of slip planes with the crystal surface. For the common case of the (001) growth of semiconductors with fcc lattices (e.g., $\text{Si}_{1-x}\text{Ge}_x$ on Si or $\text{In}_x\text{Ga}_{1-x}\text{As}$ on GaAs), the undulating surface morphology exhibits ridges and grooves parallel to the [110] and $[\bar{1}10]$ directions on the surface. A representative crosshatch morphology is shown in Fig. 1 for a partially strain-relaxed 0.25- μm -thick $\text{In}_{0.25}\text{Ga}_{0.75}\text{As}$ layer on (001) GaAs. The crosshatch typically has peak-to-valley heights of 10–100 Å and peak-to-peak spacings of 0.1 μm to several microns depending on the mismatch, film thickness, and growth conditions.

Recently, we have proposed that crosshatch is related to the formation of misfit dislocations (MDs) and surface steps via glide of threading dislocation (TD), which is accompanied by the appearance of surface steps (also called slip steps).¹ Full details of this work were presented previously and we refer to that paper now as Part I.² It is expected that these surface steps may be eliminated to a certain degree by step motion due to mass transport on the surface during film growth or annealing. Two equal slip steps moving in the opposite direction will annihilate when they meet. (001) surfaces of zincblende semiconductors have twofold symmetry. For (001) GaAs, molecular beam epitaxy growth typically takes place on surfaces with (2×4) reconstructions. This reconstruction consists of missing As dimer rows in the $[\bar{1}10]$ direction. Experimentally, it has been established that $[\bar{1}10]$ is the fast ad-species diffusion direction and [110] is the slow diffusion direction.^{3,4} Kley *et al.* calculated a diffusional barrier of 1.2 eV in the $[\bar{1}10]$ direction and 1.5 eV in the [110] direction.⁵ Because of the difference in the diffu-

^{a)}Electronic mail: speck@mrl.ucsb.edu

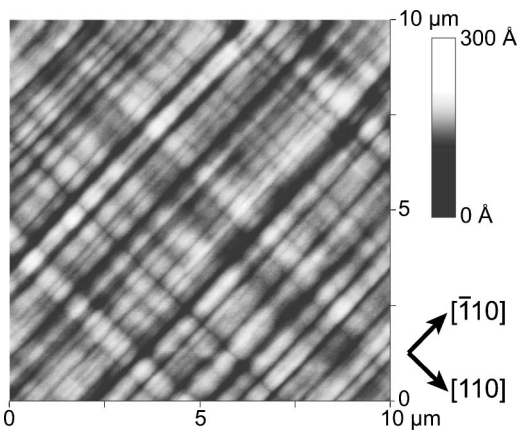


FIG. 1. Characteristic AFM image of a crosshatch pattern for a 0.25- μm -thick $\text{In}_{0.25}\text{Ga}_{0.75}\text{As}$ layer on a (001) oriented GaAs substrate.

sion coefficient in the $[110]$ and $[\bar{1}10]$ directions on the $\text{In}_{0.25}\text{Ga}_{0.75}\text{As}$ surface, the degree of step elimination should differ in the two directions.

For a quantitative understanding of crosshatch patterns, the surface morphology development was studied by means of Monte Carlo simulations in Part I. The simulation procedure was based on analytic solutions for the stress field and displacement field which appear at the film surface due to the introduction of a MD at the film/substrate interface. In the simulation, the surface profile changes due to the superposition of the normal component of the displacement from many MDs which were introduced at the film/substrate interface. Since diffusion and growth processes were not included in the model, two limiting cases of the behavior of slip steps were considered: (i) the complete absence of step motion; and (ii) the complete elimination of slip steps by step motion and annihilation. These two cases have been called “slip step only” (SSO) and “slip step eliminated” (SSE), respectively. The simulations in Part I were performed within a finite cell using analytic solutions for a laterally infinite film/substrate system. To reduce finite size effects, the stress and displacement fields of four further cells on each side of the simulation cell were superposed.

Comparison of the simulation results with experimental data showed that the proposed mechanisms can in principal explain the crosshatch pattern observed by atomic force microscopy (AFM). It was found that slip step elimination was necessary to achieve surface height profiles comparable with the experimental values for partially relaxed $\sim 0.1\text{-}\mu\text{m}$ -thick $\text{In}_{0.25}\text{Ga}_{0.75}\text{As}$ films. However, for thicker films (e.g., $1\ \mu\text{m}$), the simulated height profiles showed large height undulations for the SSE case, where we expected progressive smoothing for the SSE case for large thickness. We now believe that the results for large film thickness were impacted by the finite number of repeat cells used in adjacency to our simulation cell.

In the present article, a more accurate analysis of crosshatch formation is given, with the eventual aim of the determination of MD nucleation mechanisms in stressed semiconductor layers. The Monte Carlo simulations were improved by using rigorous periodic boundary conditions in order to

avoid artifacts by truncation errors. To this end, exact analytic solutions for the stress and displacement fields of an infinite periodic array of MDs have been derived. On the basis of these solutions, it is possible to simulate the development of physically relevant crosshatch surface morphology. A main result of the simulations is that the measured surface height profile is best described by an arrangement of groups of MDs with the same normal component of their Burgers vector.

II. BACKGROUND

In this article, we consider cube-on-cube epitaxy of materials with fcc lattices. We use the same formalism as developed in Part I. Within the body of the text we take the x and z axes are parallel to the film/substrate interface and the y axis is perpendicular to the film/substrate interface. The x and z axes coincide with the orthogonal MD line directions. For (001) oriented semiconductors with face-centered-cubic lattices (e.g., zinc blende or diamond cubic structures), the x and z directions are parallel to $\langle 110 \rangle$ directions. The lattice mismatch is given as ϵ_m :

$$\epsilon_m = \frac{a_s - a}{a}, \quad (1)$$

where a_s and a are the substrate and relaxed film cubic lattice constants. For the case of equibiaxial mismatch, the stress state in the film is given as

$$\sigma_{xx} = \sigma_{zz} = 2G \frac{1 + \nu}{1 - \nu} \epsilon_m, \quad (2)$$

where G and ν are the shear modulus and Poisson’s ratio, respectively. For simplicity, the elastic properties of the film and substrate are assumed to be isotropic and we use the same elastic constants for the film and substrate.

The stored elastic energy w per unit area of the film/substrate interface associated with the misfit stresses is proportional to the film thickness h . Increasing the stored energy with increasing film thickness h will eventually lead to the onset of strain relaxation. MD generation at the interface between the film and substrate has been shown to be the most common mechanism for the relaxation of elastic stress.^{6–9} In the majority of cases the MDs are associated with TDs, which are concomitant to MDs but have their lines going through the film to the free surface.^{8,10} The Matthews–Blakeslee¹¹ critical thickness h_c for MD generation may be derived⁸ by considering the energetics of a combined MD–TD configuration in a stressed film

$$h_c = \frac{b}{\epsilon_m(1 + \nu)8\pi \cos \lambda} (1 - \cos^2 \beta) \ln \left(\frac{\alpha_0 h_c}{b} \right) \approx \frac{b}{\epsilon_m}, \quad (3)$$

where $b = |\mathbf{b}|$ is the magnitude of the dislocation Burgers vector \mathbf{b} , λ is the angle between the Burgers vector and a line that lies in the film/substrate interface normal to the MD line, β is the angle between the MD line and \mathbf{b} , and α_0 is the dislocation core cutoff parameter.

For a completely relaxed film, the linear density of MDs $\rho_{\text{MD,relaxed}}$ multiplied by the edge component of the MD Burgers vector parallel to the interface $b_{\parallel} = b \cos \lambda$, is equal to the misfit strain ε_m , i.e.:

$$\rho_{\text{MD,relaxed}} b_{\parallel} = \varepsilon_m. \quad (4)$$

For films of finite thickness that are grown on semi-infinite substrates, the equilibrium linear MD density $\rho_{\text{MD,equl}}$ depends on the film thickness as follows:¹²

$$\rho_{\text{MD,equl}} = \rho_{\text{MD,relaxed}} \left(1 - \frac{h_c}{h} \right), \quad h > h_c. \quad (5)$$

The actual MD density realized at a particular stage of the film relaxation is almost always less than those given by Eqs. (4) and (5) $\rho_{\text{MD,actual}} \leq \rho_{\text{MD,equl}} < \rho_{\text{MD,relaxed}}$. The extent of strain relaxation R can be therefore defined as

$$R = \frac{\rho_{\text{MD,actual}}}{\rho_{\text{MD,relaxed}}} \quad (6)$$

Figure 2 illustrates the crystallography for dislocation-assisted strain relaxation in the film growth on (001) oriented substrates. The relaxation occurs by TD motion and MD formation on the inclined glide planes.⁸ For semiconductor materials, such as $\text{Si}_{1-x}\text{Ge}_x$ and $\text{In}_x\text{Ga}_{1-x}\text{As}$, the most common slip system is $\frac{1}{2} \langle 110 \rangle \{111\}$, where a is the film lattice parameter. The Burgers vectors for this system are of the type $\frac{1}{2} \langle 110 \rangle$. They are directed along the face diagonals of the cubic cell and are the shortest possible primitive translation vectors. The set of possible Burgers vectors can be constructed by considering the edges of a half-octahedron, as shown in Fig. 2(b). The half-octahedron is oriented such that its square base is parallel to the (001) plane. For instance, if the dislocation glide plane is $(\bar{1}11)$, which is inclined with respect to the film/substrate interface by the angle $\alpha = \cos^{-1}(1/\sqrt{3}) \approx 54.7^\circ$, then the MD will have a $[110]$ line direction. For this example, if the Burgers vector $\mathbf{b} = \frac{1}{2}[0\bar{1}1]$ with $b = |\mathbf{b}| = a/\sqrt{2}$, where a is the lattice parameter of the unit cell, the MD is a mixed 60° dislocation. Such mixed misfit dislocations with their lines laying at (001) film/substrate interface are typical for heteroepitaxy of semiconductors with fcc crystal lattice.^{7,9} The orientation of the dislocation line and Burgers vector leads to $\lambda = \beta = 60^\circ$ in Eq. (3). The dislocation Burgers vector can be decomposed into edge \mathbf{b}_{edge} and screw $\mathbf{b}_{\text{screw}}$ components as shown in Fig. 2(b). Consequently, the edge component can be decomposed into parts parallel \mathbf{b}_{\parallel} and perpendicular \mathbf{b}_{\perp} to the film/substrate interface: $\mathbf{b}_{\text{edge}} = \mathbf{b}_{\parallel} + \mathbf{b}_{\perp}$. The absolute values of the above components and subcomponents are

$$|\mathbf{b}_{\text{screw}}| = b_{\text{screw}} = \frac{b}{2} = a \frac{\sqrt{2}}{4}, \quad (7a)$$

$$|\mathbf{b}_{\text{edge}}| = b_{\text{edge}} = b \frac{\sqrt{3}}{2} = \frac{a}{2} \sqrt{\frac{3}{2}}, \quad (7b)$$

$$|\mathbf{b}_{\parallel}| = b_{\parallel} = \frac{b}{2} = a \frac{\sqrt{2}}{4}, \quad (7c)$$

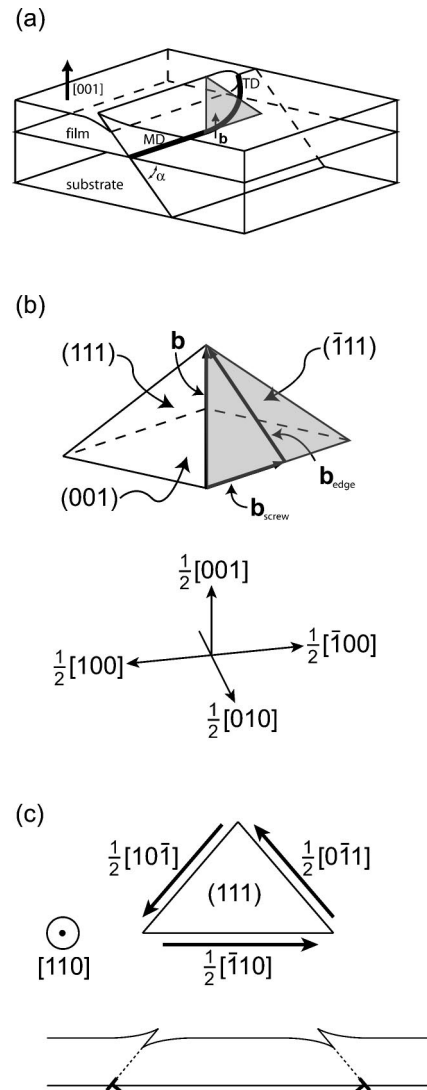


FIG. 2. The geometry for TD motion in a strained film with fcc crystal structure. (a) TD gliding on a $\{111\}$ slip plane with trailing MD, which appears at film/substrate interface as a result of TD motion. (b) Dislocation Burgers vector decomposition into the edge and screw components. (c) Projection down the $[110]$ direction, showing both the $(\bar{1}11)$ and $(1\bar{1}1)$ slip planes in projection. Glide on $(1\bar{1}1)$ with $\mathbf{b} = \frac{1}{2}[10\bar{1}]$ results in a down-step (see the slip step on the left side of the schematic). Glide on $(\bar{1}11)$ with $\mathbf{b} = \frac{1}{2}[0\bar{1}1]$ results in an up-step (see the slip step on the right side of the schematic).

$$|\mathbf{b}_{\perp}| = b_{\perp} = \frac{b}{\sqrt{2}} = \frac{a}{2}. \quad (7d)$$

For this example $\mathbf{b}_{\text{screw}} = \frac{1}{4}[\bar{1}\bar{1}0]$, $\mathbf{b}_{\text{edge}} = \frac{1}{4}[1\bar{1}2]$, $\mathbf{b}_{\parallel} = \frac{1}{4}[1\bar{1}0]$, and $\mathbf{b}_{\perp} = \frac{1}{2}[001]$. The decomposition of the MD Burgers vector, as described here, will be used in Sec. IV for the modeling of crosshatch formation.

III. EXPERIMENT PROCEDURE AND OBSERVATIONS

In the present work, epitaxial films of $\text{In}_{0.25}\text{Ga}_{0.75}\text{As}$ on GaAs (001) semi-insulating substrates were investigated. The InGaAs layers were grown by molecular beam epitaxy at 500–520 °C and were produced by concurrent Ga and In

fluxes. The film thickness of the three samples shown in this report were $h=0.1, 0.25,$ and $1.0 \mu\text{m}$. The lattice mismatch for $\text{In}_{0.25}\text{Ga}_{0.75}\text{As}$ on GaAs is 1.8% and the critical thickness h_c for this mismatch is $\sim 50 \text{ \AA}$ [see Eq. (3)] for this composition. Consequently, the film thicknesses were also approximately $20, 50,$ and $200 h_c$. The surface height profiles of the InGaAs films were determined by AFM in tapping mode (Digital Instruments Dimension or Nanoscope).

The extent of strain relaxation and the film composition were determined by measuring the separation of the film and substrate peak for (115) and $(\bar{1}\bar{1}5)$ reflections in double crystal high-resolution x-ray measurements (for details of this technique see Ref. 13). Significant strain relaxation ($R > \sim 0.05$) was observed for $h \sim 10h_c = 500 \text{ \AA}$. The magnitude of the relaxation was always smaller than the equilibrium value (see Part I for further details). For instance, 1000- \AA -thick films ($\sim 20h_c$) were $\sim 70\%$ strain relaxed whereas the equilibrium relaxation at this thickness is $\sim 95\%$.

The crosshatch morphology typically shows a strong anisotropy in III-V semiconductors, as shown in Fig. 1. Generally, the crosshatch shows larger height undulations in the $[110]$ direction than in the $[\bar{1}\bar{1}0]$ direction. As discuss earlier, $[\bar{1}\bar{1}0]$ is the fast diffusion direction on (001) GaAs surfaces and $[110]$ is the slow diffusion direction. Figures 3 and 4 show measured surface height profiles in the $[110]$ and $[\bar{1}\bar{1}0]$ directions, respectively, for 0.1- and 0.25- μm -thick films. In both the $[110]$ and $[\bar{1}\bar{1}0]$ directions, the crosshatch amplitude increases with increasing film thickness.

For a better characterization of the surface height profile, the one-dimensional height-height correlation function of a surface cross section was calculated. It is defined as

$$C(r) = \langle [h(x) - \bar{h}][h(x+r) - \bar{h}] \rangle_x, \quad (8)$$

where $h(x)$ is the surface height at a point x , $\bar{h} = \langle h(x) \rangle_x$ is the average height, and $\langle \dots \rangle_x = (1/L) \int_0^L \dots dx$ is an average over the lateral sample length L . The height profile is actually given only at discrete points x_i both in the measurement and in the simulations. Thus, the correlation function was calculated as

$$C(r) = \frac{1}{N} \sum_{i=1}^N [h(x_i) - \bar{h}][h(x_i+r) - \bar{h}], \quad (9)$$

where N is the number of data points and r is the distance between two points x_i and x_j . The correlation function $C(r)$ reflects the overall patterning of the hills and valleys in the considered direction on the surface. $C(r=0)$ is just the variance of the surface height, i.e., the square of the rms roughness of the analyzed length interval.

The height-height correlation function resulting from the experimental profiles reveals characteristic correlation lengths. The height-height correlation function for the experimental profiles shows clear correlations in the hill and valley structure. In the $[110]$ direction [Fig. 3(c)], the first peak-to-peak spacing of $C(r)$ increases from ~ 0.5 to $\sim 0.7 \mu\text{m}$ and the amplitude of $C(r)$ also increases with increasing film thickness. In the $[\bar{1}\bar{1}0]$ direction [Fig. 4(c)], the 0.1- μm -

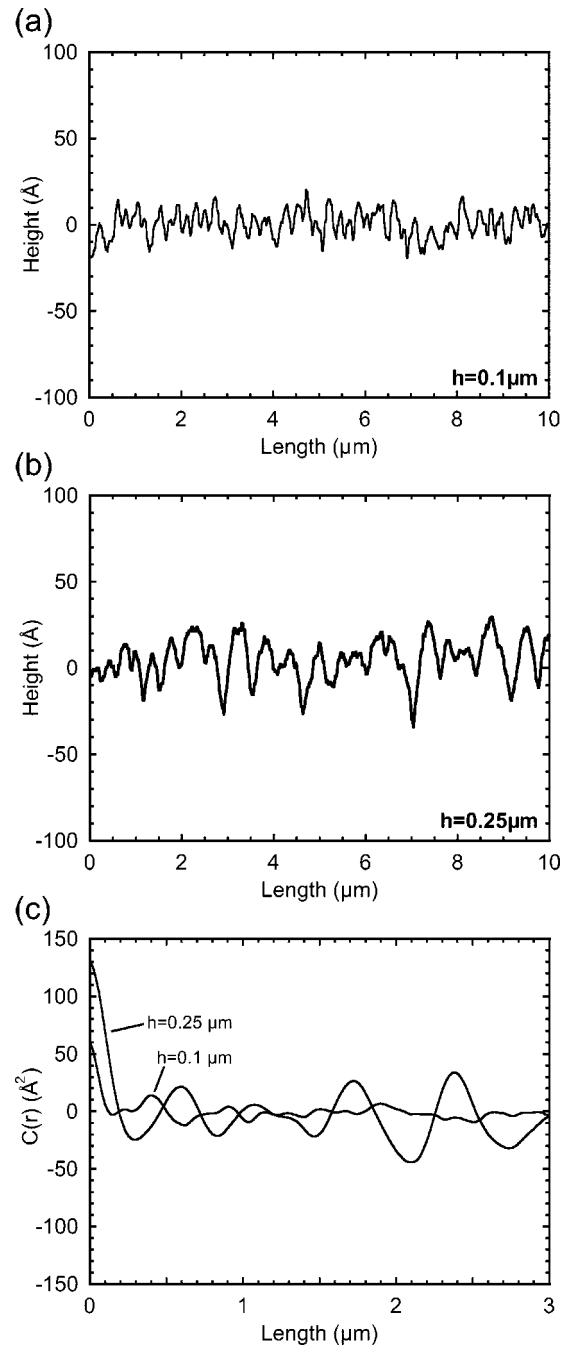


FIG. 3. Height profiles, from AFM images of $\text{In}_{0.25}\text{Ga}_{0.75}\text{As}/\text{GaAs}$ films, along the $[110]$ direction. (a), (b) Sample surface profiles for 0.1- and 0.25- μm -thick films, respectively. (c) Height-height correlation functions for profiles shown in parts (a) and (b).

thick sample shows small height variation whereas the 0.25- μm -thick sample shows more characteristic crosshatch [see the line scan in Fig. 4(b)].

IV. THEORETICAL MODEL AND SIMULATION RESULTS

A. Misfit dislocation formation at the film/substrate interface

As a first step, we briefly describe the basis of our model for crosshatch development proposed in Part I. The model examines the creation of surface steps arising from the glide

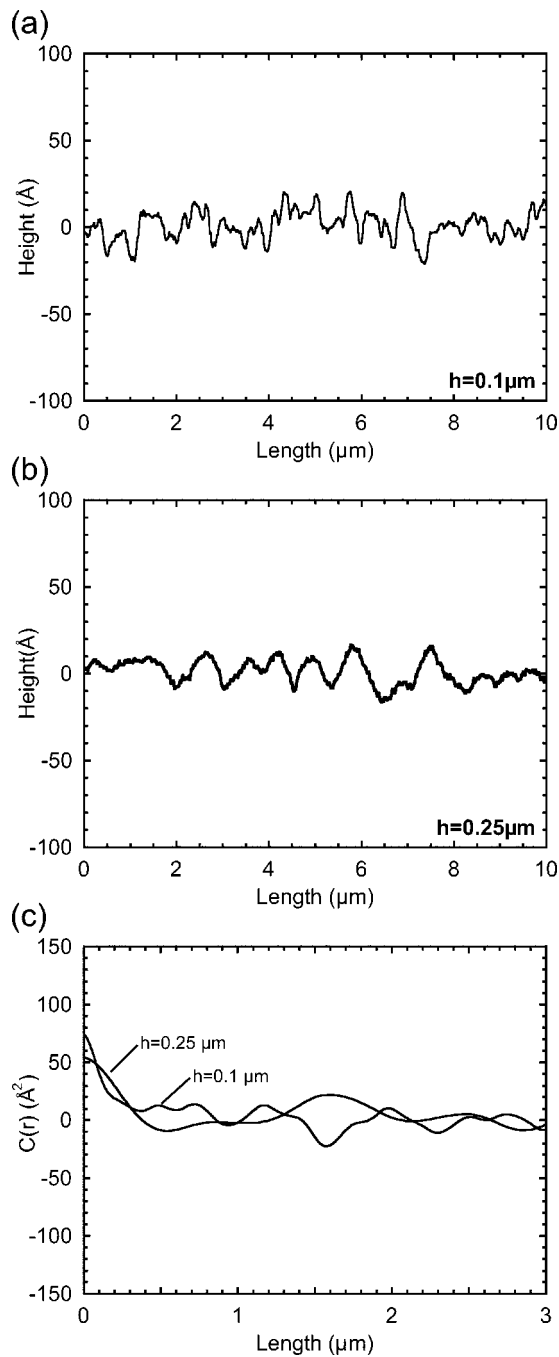


FIG. 4. Height profiles, from AFM images of $\text{In}_{0.25}\text{Ga}_{0.75}\text{As}/\text{GaAs}$ films, along the $[\bar{1}10]$ direction. (a), (b) Sample surface profiles for $h=0.1$ and $0.25 \mu\text{m}$, respectively. (c) Height–height correlation functions for profiles shown in parts (a) and (b).

of TDs along opposing $\{111\}$ slip planes, as shown schematically in Fig. 2(c), and the consequent development of MDs at the film/substrate interface. We note that only the MDs Burgers vector edge component parallel to the film/substrate interface \mathbf{b}_{\parallel} can contribute to strain relaxation in mismatched layers (assuming equibiaxial stress). The same component of \mathbf{b}_{\parallel} can be realized with different orientation Burgers vectors. For instance, MDs with $[110]$ line direction can be generated either via glide of TDs with $\mathbf{b}=\frac{1}{2}[0\bar{1}1]$ on $(\bar{1}11)$ or glide of TDs with $\mathbf{b}=\frac{1}{2}[10\bar{1}]$ on $(1\bar{1}1)$, as shown in Fig. 2(c). In both cases, $\mathbf{b}_{\parallel}=\frac{1}{4}[1\bar{1}0]$. However, for this example, glide on

$(\bar{1}11)$ corresponds to $\mathbf{b}_{\perp}=\frac{1}{2}[001]$ and glide on $(1\bar{1}1)$ corresponds to $\mathbf{b}_{\perp}=\frac{1}{2}[00\bar{1}]$. When viewed along the $[110]$ direction and taking the positive x -direction parallel to $[\bar{1}10]$, then the slip step associated with glide on $(\bar{1}11)$ corresponds to an “up-step” and glide on $(1\bar{1}1)$ corresponds to a “down-step,” as shown in Fig. 2(c). In the context of Fig. 2(c), we designate dislocations gliding on $(1\bar{1}1)$ as “left” dislocations and those gliding on $(\bar{1}11)$ as “right” dislocations.

Figure 5(a) shows the geometry used for the one-dimensional Monte Carlo simulations in Part I. Dislocations were randomly introduced at the possible nucleation sites at the surface [shown as ticks in Fig. 5(a)] and were then assumed to glide until they reached the film/substrate interface. While the nucleation sites could be located at every lattice site ($\sim 4 \text{ \AA}$ apart), we used a larger spacing of 20 \AA . The angle of the glide direction $[\alpha = \pm \cos^{-1}(\sqrt{1/3}) = \pm 54.74^{\circ}]$ was also randomly selected for each dislocation, with some dislocations gliding left and some right, with equal numbers of the two types to keep a net Burgers vector of zero. More than one dislocation was allowed at each site. Dislocations were added until either the average stress reached a prescribed value or until a set number of dislocations was reached to achieve a relaxed film. The misfit strain ($\epsilon_m = 1.8\%$) was taken to match that of $\text{In}_{0.25}\text{Ga}_{0.75}\text{As}$, leading to a relaxed film with 866 MDs per $10 \mu\text{m}$ length with a mean dislocation spacing of about 115 \AA . The surface height was calculated from the displacement fields of the dislocations. In Part I, linear elasticity was used to calculate the surface profile associated with a single MD placed at film/substrate interface, such that the net surface displacement was a superposition of the displacements from individual dislocations. We introduced and explored two limiting cases for the formation of cross-hatch: SSO case and SSE case. For the SSO case the surface profile was assumed to be related entirely with steps formed by dislocation glide from the film surface modulated by MD elastic field. The SSE case corresponds to complete elimination of the surface steps in the considered computational cell, as would be realized by step annihilation during growth. Mathematically the SSE case was realized by adding the step-like heaviside function to the displacement determined for SSO case (for detail please refer to Part I). Periodic boundary conditions were approximated by considering the fields from the simulation cell and four replica cells on each side of the central cell. Surface heights were calculated for the SSE and SSO cases for a range of film thicknesses h and were compared with experiment.

There was a serious limitation to the earlier model owing to the truncation of the displacement fields of MDs at a finite number of periods. Elastic fields from dislocation fields are long range and thus the use of truncated solutions can be problematic for large film thicknesses compared with the period of the computational cell. In the present article, we have solutions (see the Appendix) for infinitely periodic arrays of dislocations and thus can eliminate truncation errors.

The compressive stress σ_{xx} at the film surface, arising from an infinite periodic array of MDs at the film/substrate interface, was derived from Eqs. (A15b) and (A16b) with properly transformed coordinates

$$\sigma_{xx} = \frac{Gb_{\parallel}}{(1-\nu)} \frac{4\pi \frac{h}{l} \left[1 - \cos\left(2\pi \frac{x}{l}\right) \cosh\left(2\pi \frac{h}{l}\right) \right] - 2 \sinh\left(2\pi \frac{h}{l}\right) \left[\cos\left(2\pi \frac{x}{l}\right) - \cosh\left(2\pi \frac{h}{l}\right) \right]}{l \left[\cos\left(2\pi \frac{x}{l}\right) - \cosh\left(2\pi \frac{h}{l}\right) \right]^2} \pm \frac{Gb_{\perp}}{(1-\nu)} \frac{4\pi h \sin\left(2\pi \frac{x}{l}\right) \sinh\left(2\pi \frac{h}{l}\right)}{l^2 \left[\cos\left(2\pi \frac{x}{l}\right) - \cosh\left(2\pi \frac{h}{l}\right) \right]^2}, \tag{10}$$

where we assume that one MD from the array is placed at the position $(0, -h)$, the array period is l , $b_{\perp} = b/\sqrt{2} = a/2$ and $b_{\parallel} = b/2 = a\sqrt{2}/4$ with the sign “+” or “-” corresponding to the left or right MD, respectively. In Fig. 5(b) we show σ_{xx} for a periodic array of MDs in a film with thickness $h = 100b$ and repeat period $l = 2500b$. The total stress in the film after introducing the fixed number of MDs is given by the summation of the individual contributions given by Eq. (10).

The displacement component u_y (i.e., normal component of the displacement) at the surface (for the SSO case) of the periodic MD array was derived from Eqs. (A10a) and (A11a):

$$u_y = b_{\parallel} \frac{h}{l} \frac{\sinh\left(2\pi \frac{h}{l}\right)}{\left[\cos\left(2\pi \frac{x}{l}\right) - \cosh\left(2\pi \frac{h}{l}\right) \right]} \mp b_{\perp} \left\{ \frac{1}{\pi} \tan^{-1} \left[\cot\left(\pi \frac{x}{l}\right) \tanh\left(\pi \frac{h}{l}\right) \right] + \frac{h}{l} \frac{\sin\left(2\pi \frac{x}{l}\right)}{\left[\cos\left(2\pi \frac{x}{l}\right) - \cosh\left(2\pi \frac{h}{l}\right) \right]} \right\}. \tag{11}$$

The displacement for the case with step elimination can be found by adding a step-like function to the solution given by Eq. (11). The step of the height b_{\perp} is added to left boundary of the computational cell for the right nucleated MD and to the right boundary for the left nucleated MD. In Fig. 5(c), there is a sharp spike in the displacement profile associated with a surface step (the SSO case), while in Fig. 5(d) we see the more uniform displacement found when either growth or diffusive transport have eliminated the step (SSE). In Figs. 11 and 12 in the Appendix, we compare displacements and stresses, respectively, for the infinitely periodic system and those from a single, nonperiodic, MD.

B. Simulated surface profiles

Figure 6 presents calculated surface profiles for three film thicknesses ($h = 0.1, 1.0,$ and $10 \mu\text{m}$) based on a random

placement of dislocations at the nucleation sites of Fig. 5(a) and with a net Burgers vector of zero. Results are shown for both the SSO and SSE limits. The distribution of dislocations was the same in all plots. The corresponding height-height correlation functions $C(r)$ are shown in Fig. 7. In Fig. 6(a), we see that the surface profile in the SSO case for a thickness of $h = 0.1 \mu\text{m}$ produces a film that is microscopically rough, but mesoscopically smooth, which is verified by the flat height-height correlation function $C(r)$ in Fig. 7(a). As the thickness is increased, the SSO surface becomes increasingly rough [Figs. 6(b) and 6(c)] owing to the broadening of the stress and displacement fields at increasing thickness. By $h = 10 \mu\text{m}$, the SSO surface is extremely rough, with complete surface steps that resemble stacked monolayers. In Fig. 7(a), we see that there is a broadening of the height-height correlation with thickness, but with no real structure, as expected from random surfaces. The long wavelength undulation in the height-height correlation function $C(r)$ for the $h = 10 \mu\text{m}$ case is the result of presenting a single realization of the system—if averages over many runs were shown, the $C(r)$ would be flat for all thickness, as expected for random surfaces.

When the slip steps are eliminated by diffusive transport or growth (SSE case), the local morphology is smooth for thin films with a long mesoscale undulation [Figs. 6(a) and 7(b)]. As the film thickness increases, the SSE film becomes mesoscopically smoother until it is perfectly flat at $h = 10 \mu\text{m}$ [Figs. 6(c) and 7(b)]. Once again, this behavior is expected for a random distribution of dislocations.

The surface height profiles were also calculated for groups of MDs, as shown in Fig. 8. Repeated patterns of n left dislocations and n right dislocations were placed in the one-dimensional simulation cell, with n varying from 12 to 48 such that the MD-MD spacing corresponds to a fully relaxed $\text{In}_{0.25}\text{Ga}_{0.75}\text{As}$ film. Thus, the repeat periods $2n = 24, 48,$ and 96 correspond to lateral dimensions of $\sim 0.28, 0.56,$ and $1.12 \mu\text{m}$, respectively. The surface height was calculated in each case for both the SSO and SSE limits as a function of film thickness. In the hypothetical case in which the MDs group size is larger than the film thickness, as illustrated in Fig. 8(a) ($n = 12$ case for a $0.01\text{-}\mu\text{m}$ -thick film), we see that the SSE case gives rise to large hills and valleys whereas the SSO surface shows slight undulations and atomic-scale roughness. This result is consistent with our earlier interpretation of crosshatch.^{1,2} When the film thickness is comparable or much larger than the group [see Figs.

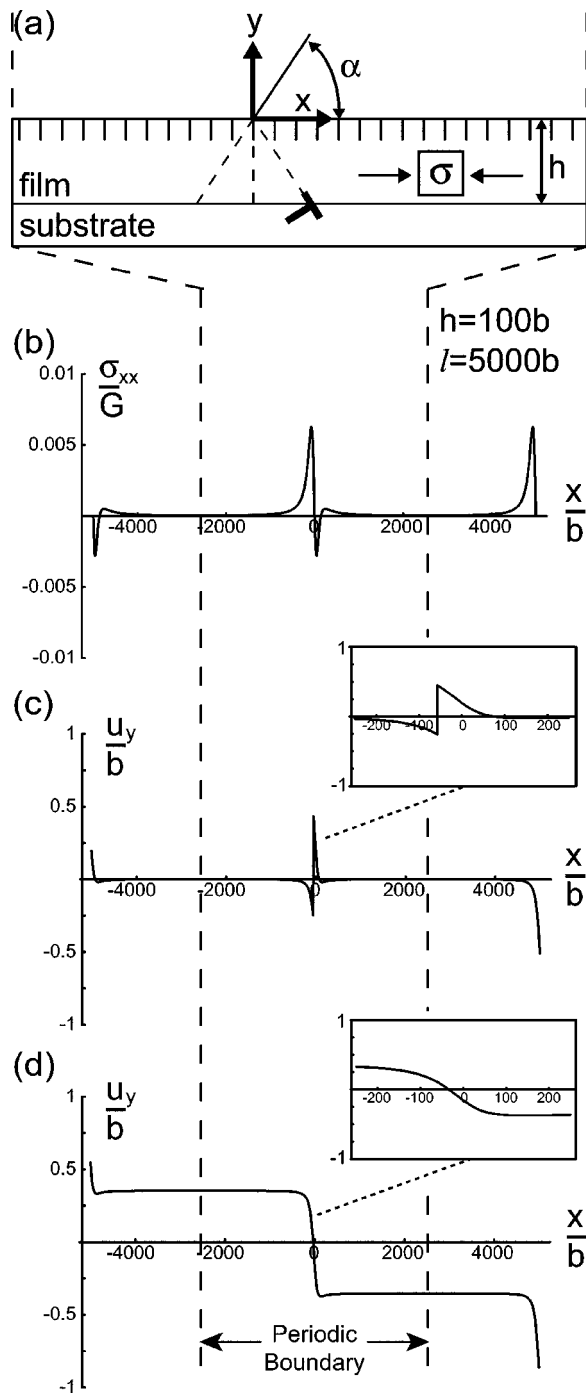


FIG. 5. One-dimensional model for dislocation assisted strain relaxation in mismatched films. (a) Schematic for showing the geometry used for introducing dislocations into the strained film. (b) Example of analytical solution for stress σ_{xx} at the film surface due to the periodic array of MDs. (c) Example of analytical solution for displacement u_y at the film surface. The displacement profile includes the surface step created as a result MD introduction via TD motion; referred to as SSO case. (d) Example of analytical solution for displacement u_y at the film surface with the surface step removed. The displacement profile resembles the effect of surface step elimination from lateral mass transport; referred to as SSE case. For the plots in parts (b)–(d) b is the magnitude of the full dislocation Burgers vector; the film thickness was taken as $h=100b$; the periodic spacing between dislocations was $l=2500b$; Poisson's ratio $\nu=0.32$.

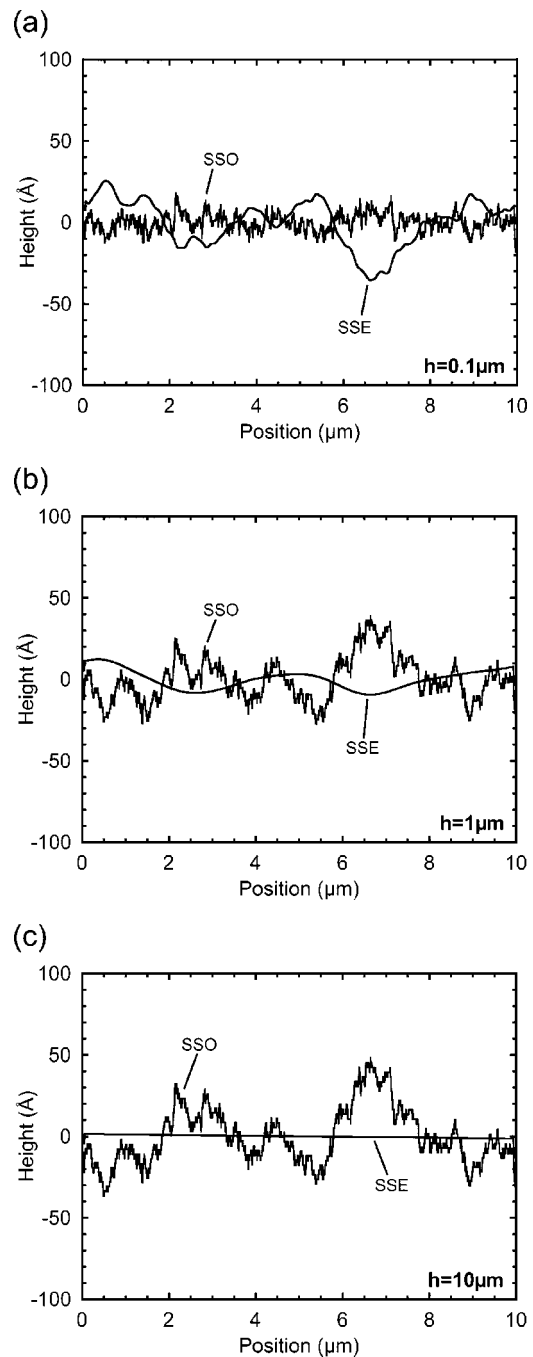


FIG. 6. Surface profiles for the model with randomly nucleated dislocations. (a), (b), and (c) Surface height profiles for $h=0.1$, 1.0 , and $10 \mu\text{m}$, respectively. The modeled film composition $\text{In}_{0.25}\text{Ga}_{0.75}\text{As}$ corresponds to $\nu=0.32$, and $\epsilon_m=1.8\%$; 100% strain relaxation corresponds to 866 dislocations for $10 \mu\text{m}$ of film length.

8(b) and 8(c) for $n=12$ and $h=0.1$ and $1.0 \mu\text{m}$, respectively] we find that the behavior reverses and the SSE cases show smaller height undulations than the SSO cases. This is expected, as with increasing film thickness the SSE cases correspond to “filling” of the valleys with material from the peaks. Figure 8(d) shows the amplitude of the peak oscillations (peak-to-valley height) for a film thickness from 0.01 to $1.0 \mu\text{m}$ for both the SSO and SSE cases for $n=12$, 24 , and 48 . Note that the SSE surface is essentially flat when the film thickness is comparable to the repeat period of the MD

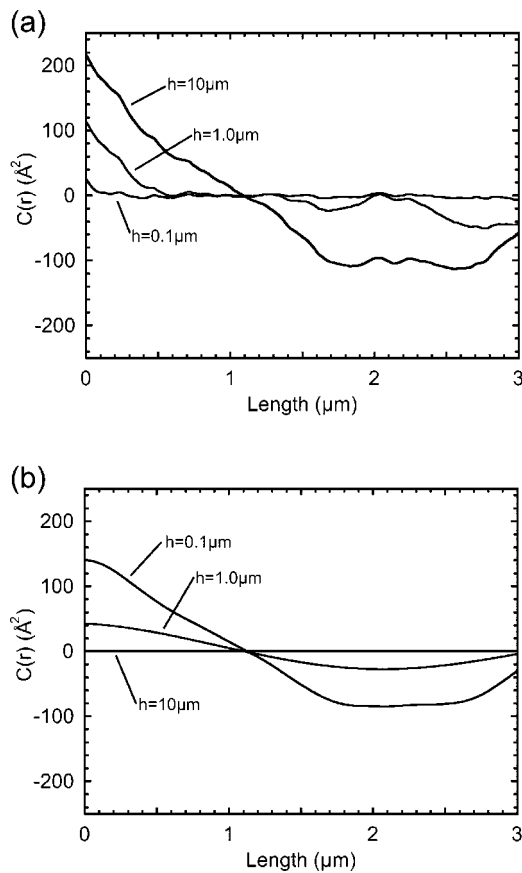


FIG. 7. Height–height correlation functions $C(r)$ for surface profiles in the model with randomly nucleated dislocation for SSO (a) and SSE (b) cases for different film thicknesses. The data correspond to a fully relaxed $\text{In}_{0.25}\text{Ga}_{0.75}\text{As}$ layer with $\nu=0.32$, and $\epsilon_m=1.8\%$.

groups. In contrast, for the system with no diffusion (SSO), the amplitude increases both with increasing film thickness and with the increasing repeat period of the MDs. There is an approximately linear correlation between period and surface amplitude for the 1- μm -thick films.

In Fig. 9(a) we show an AFM image for a 1 μm film of $\text{In}_{0.25}\text{Ga}_{0.75}\text{As}$ grown at 520 $^\circ\text{C}$. This film showed the characteristic undulating crosshatch pattern in the $[110]$ direction and weak patterns in the orthogonal $[\bar{1}10]$ direction, as shown in the line scans in Fig. 9(b). From the height–height correlation function [Fig. 9(c)], the peak-to-peak spacing is at a distance of $\sim 1.25 \mu\text{m}$ along the $[110]$ direction with a peak-to-valley height of $\sim 100 \text{ \AA}$ [the measured averaged peak-to-valley height was 103.5 \AA for the line scan shown in Fig. 9(b)]. In contrast, the peak-to-peak height is at a distance of $\sim 2.5 \mu\text{m}$ along the $[\bar{1}10]$ direction with a peak-to-valley height of $\sim 20 \text{ \AA}$. Based on Fig. 8, the experimental result can be interpreted as showing that the undulating surface height profile in the $[110]$ direction is due to groups of MDs with little or no step elimination (SSO case). In contrast, the surface profile in the $[\bar{1}10]$ direction is smooth and suggests that the surface steps have been eliminated via lateral transport during growth. We note that the results for the SSE case in Fig. 8 demonstrate that the film thickness must be comparable to the wavelength of the group period to re-

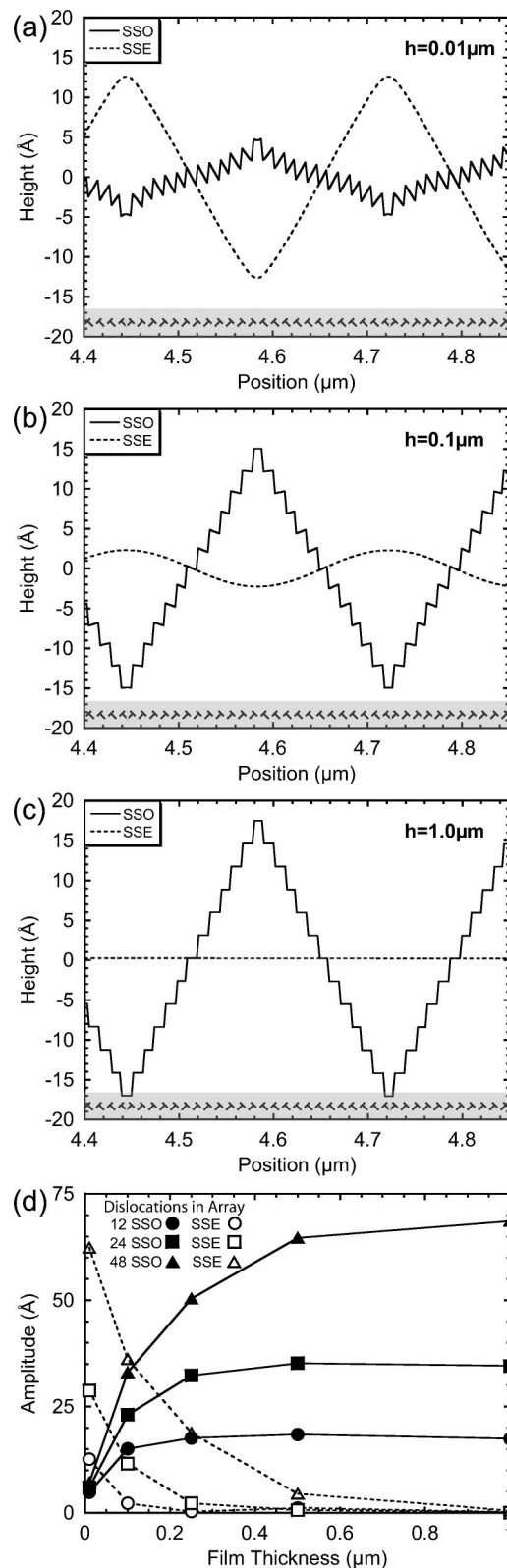


FIG. 8. Surface displacement from dislocation group arrays. (a), (b), and (c) Surface profile for a periodic array of 12 similar dislocation in the period for $h=0.01, 0.1,$ and $1.0 \mu\text{m}$, respectively. The schematic for dislocation groups is also shown in the bottom of each part. (d) Surface profile amplitude vs film thickness for dislocation arrays of 12, 24, and 48 dislocations. The SSO case is shown with solid markers and the SSE case with open markers.

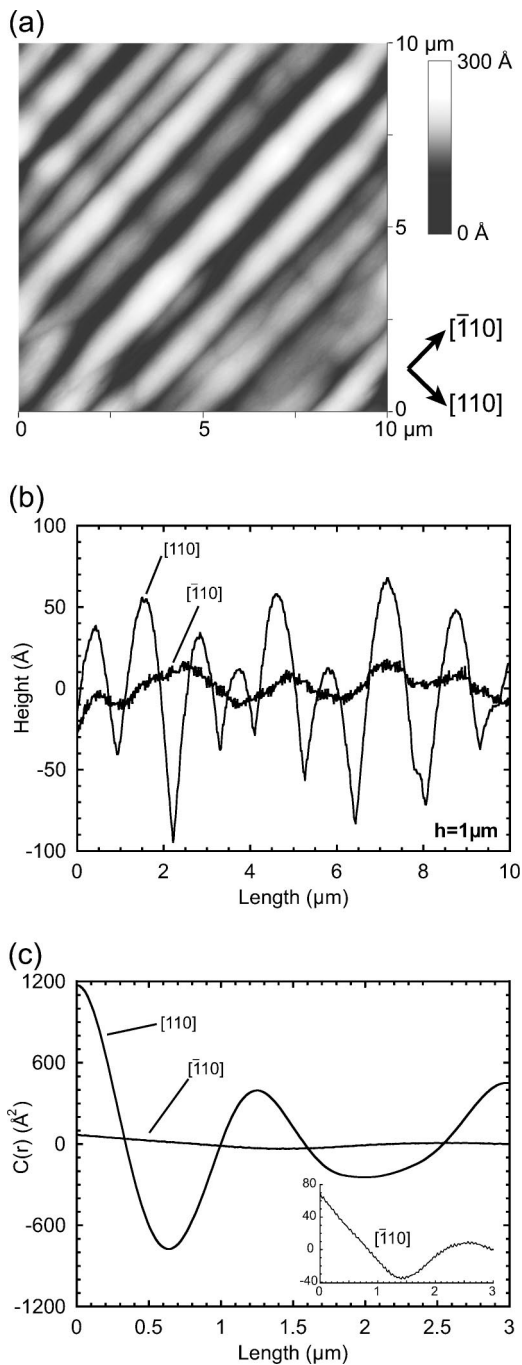


FIG. 9. Example of strongly anisotropic crosshatch pattern in $h=1\ \mu\text{m}$ $\text{In}_{0.25}\text{Ga}_{0.75}\text{As}$ layer on a (001) oriented GaAs substrate. (a) AFM image showing the crosshatch pattern. (b) Line scans of the AFM image in the $[110]$ and $[\bar{1}10]$ direction. (c) Height–height correlation functions in the $[110]$ and $[\bar{1}10]$ direction.

alize a flat surface. Thus, the slight undulations in the $[\bar{1}10]$ direction may be possibly due to the relatively large wavelength of the undulation ($\sim 2.5\ \mu\text{m}$) in comparison with the film thickness ($1\ \mu\text{m}$). We should make clear, however, that this is only a speculative conclusion as the MDs orthogonal to the $[\bar{1}10]$ direction may have a more random distribution in their normal component.

V. DISCUSSION

In this article, we have implemented solutions for the stress fields and displacements for infinite arrays of MDs for

the calculation of crosshatch morphologies. These solutions now provide the expected behavior for the surface profiles for all film thicknesses. As shown in Part I (see Fig. 5 of Part I), the film thickness is the characteristic lateral “decay” length for either the stress field or displacement field for a single MD; i.e., the far-field elastic fields or displacement fields for a MD are only asymptotically realized at lateral dimensions many times the film thickness. Thus, the solutions for truncated MD arrays used in Part I were excellent approximations for thin films (e.g., $1000\ \text{\AA}$), however, the solutions did not present the expected behavior for thicker films (e.g., $1\ \mu\text{m}$). Using the fully periodic solutions, the surfaces become smoother with increasing film thickness for the SSE case, as shown in Fig. 6 for the case of randomly introduced MDs and Fig. 8 for MD groups. In contrast, the roughness for the SSO case increases with film thickness, either due to random groups (Fig. 6) or periodic groups (Fig. 8) and then remains essentially constant at film thicknesses comparable or larger than the lateral MD group size.

MD groups provide an easy way to understand the surface profile at large film thicknesses. Consider groups of n left MDs and n right MDs, as shown in Fig. 8, in the SSO case the n left MDs correspond to n down-steps (considering the height profile from left to right in all figures in this article) and the n right MDs correspond to n up-steps. In the SSO case, these n up-steps and n down-steps persist at all film thicknesses. When the film thickness is large in comparison with the period of the MDs ($2n$ MDs), the displacement field from an individual MD spreads, as shown in Fig. 11, however, there is still a discrete step in the SSO case. Thus, the surface height profile at large film thicknesses is essentially given by the addition of n negative heaviside step functions (down-steps) and n positive heaviside step functions (up steps)—each positioned at intersection of the slip plane of the MD with the free surface. In contrast, the surface height profile from an individual MD in the SSE case broadens with increasing film thickness. When the film thickness becomes large in comparison to the MD group size ($2n$ MDs), then the displacements cancel and the surface is flat. Figure 8(d) shows that the peak-to-valley height will increase with increasing film thickness in the SSO case (in contrast, the peak-to-valley height follows the opposite trend in the SSE case). Thus, for relaxed films, the change in the surface profile with increasing film thickness should be a strong indicator of whether the crosshatch morphology is more appropriately described by the SSO or SSE cases. In the $[110]$ direction [see Figs. 3(c) and 9(c) of this article and Fig. 3(b) of Part I], the surface height undulations increase with increasing film thickness. Thus, we conclude that the morphology in the $[110]$ direction is associated with groups of MDs with period at least as large as the film thickness. In the $[\bar{1}10]$ direction, the trend in the height profile with increasing film thickness evolution is less clear [see Figs. 4(c) and 9(c)], but we speculate that the crosshatch is reduced in this direction due to surface diffusion.

In the simulations in this article, we randomly introduced the MD location and whether the MD corresponded to an up-step or down-step (i.e., glide to the right or left, respectively). Since the MDs were randomly introduced, the

height–height correlation function $C(r)$ showed a monotonic decay with increasing distance r and no subsidiary maxima. In contrast, the experimental height–height correlation functions showed strong secondary maxima which we attribute to groups of MDs with the same normal component. We believe that these MD groups themselves are the result of either heterogeneous sources for dislocations, or multiplication processes, which result in parallel arrays of MDs with the same Burgers vector. We are currently studying the freshly desorbed surfaces of arsenic-capped $\text{In}_{0.25}\text{Ga}_{0.75}\text{As}$ layers with AFM and scanning tunneling microscopy to observe the surface structure (with a particular focus on the step structure). Our preliminary results show that the surfaces have a high step density in both the $[110]$ and $[\bar{1}10]$ directions and thus lends support that the crosshatch is largely related to the SSO case.

In general, a pronounced crosshatch can be also related to MD patterning, i.e., formation of local regions at the film/substrate interface with a high density of MDs separated by regions with a low density of MDs. Such patterning phenomena have been observed experimentally and studied in the framework of dislocation reaction-kinetic model (see Ref. 14, and references therein). However, it is clear that the energy of a nonuniform MD distribution is higher than the energy of a periodic array of MDs.¹⁵ In the analysis of MD patterning it was always assumed a pure edge character of dislocations with their Burgers vector parallel to the interface. On the other hand, consideration of left and right generated MD with opposite component of Burgers vector allows the formation of dislocation patterns with lower energy than simple nonuniform distribution of MDs. Therefore, our current efforts are also directed to the theoretical study of the energetics of such MD groups with alternating normal component of their Burgers vector.

VI. SUMMARY AND CONCLUSIONS

In this article, we have presented solutions for the stress and displacement fields for periodic MD arrays which include the effects of the free surface. These solutions were used in simulations of crosshatch formation. The surface height profiles have been simulated for periodic MD arrays of randomly introduced dislocations as well as for regular dislocation arrangements, i.e., groups of dislocations having the same component of their Burgers vector normal to the film/substrate interface. The surface height profile evolves due to the appearance of slip steps at the film surface and subsequent step motion. Two limiting cases of step motion have been modeled: extremely slow step motion (SSO case) and extremely fast step motion leading to complete step elimination (SSE case). For random MD arrangement, the rms surface roughness increases with increasing film thickness in the SSO case, whereas in the SSE case it decreases at higher film thickness. Experimentally observed surface height profiles showed a certain degree of periodicity. Therefore, they can be better described by the solutions for groups of MDs with alternating sign of the normal component of the dislocation Burgers vector. However, also for this case, the SSE limit leads to a decrease of the rms surface roughness

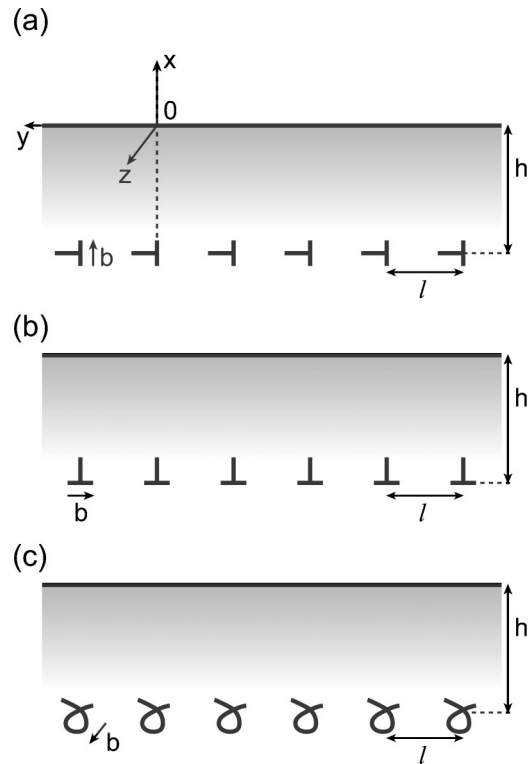


FIG. 10. Schematic for periodic dislocation arrays. (a) Edge dislocation array with Burgers vector perpendicular to the surface. (b) Edge dislocation array with Burgers vector parallel to the free surface. (c) Screw dislocation array.

with increasing film thickness. Experimentally we have found that the rms roughness of relaxed $\text{In}_{0.25}\text{Ga}_{0.75}\text{As}$ films on GaAs (001) increase with increasing film thickness in the $[110]$ direction. Thus, we conclude that the crosshatch morphology is predominantly described by the SSO case.

ACKNOWLEDGMENTS

This work was supported by DARPA (W. Coblenz program manager) and monitored by AFOSR (G. Witt).

APPENDIX: DISPLACEMENTS AND ELASTIC STRESSES OF PERIODIC DISLOCATION ARRAYS IN SUBSURFACE LAYERS

Here we present analytical expressions for displacements and elastic stresses for periodic dislocation arrays placed near a free surface of an elastically isotropic material. The geometry of the arrays is given in Fig. 10, together with the chosen right-handed coordinate system. We note that this coordinate system corresponds to that conventionally used in dislocation mechanics. However, this coordinate system differs from commonly used coordinate systems for thin films, such as we use in the body of this article. The following considers three fundamental orientations of the dislocation Burgers vector with respect to the free surface: (i) edge dislocations with Burgers vector normal to the free surface $\mathbf{b} = b_x \mathbf{e}_x$ [Fig. 10(a)]; (ii) edge dislocations with Burgers vector parallel to the free surface $\mathbf{b} = -b_y \mathbf{e}_y$ [Fig. 10(b)]; and (iii) screw dislocations with Burgers vector parallel to the free surface $\mathbf{b} = b_z \mathbf{e}_z$ [Fig. 10(c)]. b_i are the magnitudes of

the Burgers vectors and \mathbf{e}_i are the unit vectors along the corresponding coordinate axes. The dislocation line direction is \mathbf{e}_z , the arrays are at the distance h from the surface, and the dislocation spacing is l . Note that the solutions for a screw dislocation given later are not used in this article.

We start the derivation of the displacement and stresses for infinite dislocation arrays with the corresponding fields for individual dislocations calculated in a semi-infinite elastic body. The solution for stresses σ_{ij} can be found for example in references¹⁶⁻¹⁸ and satisfy the boundary condition at the free surface and also differential equilibrium conditions in the bulk

$$\sigma_{xj}(x=0,y,z)=0, \tag{A1a}$$

$$\frac{\partial \sigma_{ij}}{\partial x_j}=0. \tag{A1b}$$

In our earlier article (Part I),² the expressions for the dislocation stresses were not transformed to the appropriate coordinate system.

The solutions for displacements are not so well-known in the literature. Their derivation assumes the additional integration of strains, as it was done for an isolated edge dislocation in Refs. 2 and 19. The displacements can also be determined as a result of direct solution of the elasticity problem. We will use a different method which mimics the structure of the solutions for stresses for a dislocation near a free surface.

The stresses due to a subsurface dislocation σ_{ij} can be written as the superposition of three terms

$$\sigma_{ij} = \sigma_{ij}^\infty + \sigma_{ij}^i + \sigma_{ij}^a, \tag{A2}$$

where σ_{ij}^∞ is the stress of a dislocation in an infinite medium; σ_{ij}^i is the stress of an image dislocation, which is a mirror reflection of the real dislocation (introduction of the image dislocation fulfills part of the boundary conditions at the free surface); and an additional stress σ_{ij}^a that assures that all free-surface boundary conditions are satisfied.¹⁷ For a screw dislocation, no additional terms are needed and the complete solution is found with the inclusion of a single image dislocation.

The term σ_{ij}^a can be determined by a variety of techniques. Here we employ the method of virtual surface dislocations.²⁰ In this approach σ_{ij}^a is generated by a continuous distribution of surface dislocations

$$\sigma_{ij}^a(x,y) = \int_{-\infty}^{+\infty} f(y',h) \sigma_{ij}^\infty(x,y-y') dy', \tag{A3}$$

where the dislocation distribution function $f(y,h)$ is chosen such that the boundary conditions (A1) are satisfied. Once the distribution function is found, the dislocation displacement fields are given by equations similar in form to those for stress in Eqs. (A2) and (A3):

$$u_i = u_i^\infty + u_i^i + u_i^a \tag{A4}$$

with

$$\text{with } u_i^a(x,y) = \int_{-\infty}^{+\infty} f(y',h) u_i^\infty(x,y-y') dy'. \tag{A5}$$

In Eqs. (A4) and (A5), all terms on the right-hand side are displacements arising from dislocations in an infinite media, the forms of which can be easily derived or found in the literature. Employing the distribution functions for surface dislocations found in Ref. 20, we obtain the following displacement fields for a single dislocation placed at the position $(-h,0)$ near a free surface.

(i) For an edge dislocation with $\mathbf{b} = b_x \mathbf{e}_x$:

$$u_x^{b_x} = \frac{b_x}{2\pi} \left(\tan^{-1} \frac{x-h}{y} - \tan^{-1} \frac{x+h}{y} \right) + \frac{b_x}{4\pi(1-\nu)} \left\{ \frac{(x+h)y}{(x+h)^2+y^2} + (3-4\nu) \frac{yh}{(x-h)^2+y^2} - \frac{xy}{(x-h)^2+y^2} + 4xyh \frac{(x-h)}{[(x-h)^2+y^2]^2} \right\}, \tag{A6a}$$

$$u_y^{b_x} = \frac{b_x}{4\pi(1-\nu)} \left\{ \frac{1-2\nu}{2} \ln \frac{(x-h)^2+y^2}{(x+h)^2+y^2} - \frac{(x+h)^2}{(x+h)^2+y^2} + (3-4\nu) \frac{(x-h)h}{(x-h)^2+y^2} + \frac{x(x+h)}{(x-h)^2+y^2} - 4xh \frac{(x-h)^2}{[(x-h)^2+y^2]^2} \right\}, \tag{A6b}$$

$$u_z^{b_x} = 0, \tag{A6c}$$

where ν is the Poisson's ratio of elastically isotropic material.

(ii) For an edge dislocation with $\mathbf{b} = -b_y \mathbf{e}_y$:

$$u_x^{b_y} = -\frac{b_y}{4\pi(1-\nu)} \left\{ \frac{1-2\nu}{2} \ln \frac{(x+h)^2+y^2}{(x-h)^2+y^2} - \frac{(x+h)^2}{(x+h)^2+y^2} + 2(1-2\nu) \frac{(x-h)h}{(x-h)^2+y^2} + \frac{x^2-2xh-h^2}{(x-h)^2+y^2} + 4xh \frac{(x-h)^2}{[(x-h)^2+y^2]^2} \right\}, \tag{A7a}$$

$$u_y^{b_y} = -\frac{b_y}{2\pi} \left(\tan^{-1} \frac{x-h}{y} - \tan^{-1} \frac{x+h}{y} \right) + \frac{b_y}{4\pi(1-\nu)} \left\{ \frac{(x+h)y}{(x+h)^2+y^2} + (3-4\nu) \frac{yh}{(x-h)^2+y^2} - \frac{xy}{(x-h)^2+y^2} - 4xhy \frac{(x-h)}{[(x-h)^2+y^2]^2} \right\}, \tag{A7b}$$

$$u_z^{b_y} = 0. \tag{A7c}$$

(iii) For a screw dislocation with $\mathbf{b} = b_z \mathbf{e}_z$:

$$u_x^{b_z} = 0, \tag{A8a}$$

$$u_y^{b_z} = 0, \tag{A8b}$$

$$u_z^{b_z} = \frac{b_z}{2\pi} \left(\tan^{-1} \frac{x-h}{y} - \tan^{-1} \frac{x+h}{y} \right). \tag{A8c}$$

The displacement fields all include a characteristic dislocation term proportional to \tan^{-1} , which provides the multi-value character of dislocation displacements and accounts for the generation of plastic jumps as dislocations pass through the body of a material or of an atomic step as dislocations arrive at the material surface (for a discussion of this problem see the Appendix in Part I).

The displacement field of a periodic dislocation array is

given by the sum of contributions from the individual dislocations

$$u_i^{\text{array}} = \sum_{n=-\infty}^{n=+\infty} u_i^{\text{individual}}(x, h, y - nl). \tag{A9}$$

The summation of $u_i^{\text{individual}}$ [Eqs. (6)–(7)] in Eq. (9) can be performed analytically and yields the following results for the displacement fields of an infinite dislocation array.

(i) For an array of edge dislocations with $\mathbf{b} = b_x \mathbf{e}_x$:

$$u_x^{\Sigma b_x} = \frac{b_x}{2\pi} \left\{ \tan^{-1} [\tanh \pi(\tilde{x} - \tilde{h}) \cot \pi\tilde{y}] - \tan^{-1} [\tanh \pi(\tilde{x} + \tilde{h}) \cot \pi\tilde{y}] \right\} + \frac{b_x}{4\pi(1-\nu)} \times \left\{ \begin{aligned} &\pi(\tilde{x} + \tilde{h}) \frac{\sin 2\pi\tilde{y}}{\cosh 2\pi(\tilde{x} + \tilde{h}) - \cos 2\pi\tilde{y}} + (3 - 4\nu)\pi\tilde{h} \frac{\sin 2\pi\tilde{y}}{\cosh 2\pi(\tilde{x} - \tilde{h}) - \cos 2\pi\tilde{y}} \\ &- \pi\tilde{x} \frac{\sin 2\pi\tilde{y}}{\cosh 2\pi(\tilde{x} - \tilde{h}) - \cos 2\pi\tilde{y}} + 4\pi^2\tilde{x}\tilde{h} \frac{\sinh 2\pi(\tilde{x} - \tilde{h}) \sin 2\pi\tilde{y}}{[\cosh 2\pi(\tilde{x} - \tilde{h}) - \cos 2\pi\tilde{y}]^2} \end{aligned} \right\}, \tag{A10a}$$

$$u_y^{\Sigma b_x} = \frac{b_x}{4\pi(1-\nu)} \left\{ \begin{aligned} &\frac{1-2\nu}{2} \ln \frac{\cosh 2\pi(\tilde{x} - \tilde{h}) - \cos 2\pi\tilde{y}}{\cosh 2\pi(\tilde{x} + \tilde{h}) - \cos 2\pi\tilde{y}} - \pi(\tilde{x} + \tilde{h}) \frac{\sinh 2\pi(\tilde{x} + \tilde{h})}{\cosh 2\pi(\tilde{x} + \tilde{h}) - \cos 2\pi\tilde{y}} + (3 - 4\nu)\pi\tilde{h} \\ &\times \frac{\sinh 2\pi(\tilde{x} - \tilde{h})}{\cosh 2\pi(\tilde{x} - \tilde{h}) - \cos 2\pi\tilde{y}} + \pi\tilde{x} \frac{\sinh 2\pi(\tilde{x} - \tilde{h})}{\cosh 2\pi(\tilde{x} - \tilde{h}) - \cos 2\pi\tilde{y}} + 4\pi^2\tilde{x}\tilde{h} \frac{1 - \cosh 2\pi(\tilde{x} - \tilde{h}) \cos 2\pi\tilde{y}}{[\cosh 2\pi(\tilde{x} - \tilde{h}) - \cos 2\pi\tilde{y}]^2} \end{aligned} \right\}, \tag{A10b}$$

$$u_z^{\Sigma b_x} = 0. \tag{A10c}$$

(ii) For an array of edge dislocations with $\mathbf{b} = -b_y \mathbf{e}_y$:

$$u_x^{\Sigma b_y} = -\frac{b_y}{4\pi(1-\nu)} \left\{ \begin{aligned} &\frac{1-2\nu}{2} \ln \frac{\cosh 2\pi(\tilde{x} + \tilde{h}) - \cos 2\pi\tilde{y}}{\cosh 2\pi(\tilde{x} - \tilde{h}) - \cos 2\pi\tilde{y}} - \pi(\tilde{x} + \tilde{h}) \frac{\sinh 2\pi(\tilde{x} + \tilde{h})}{\cosh 2\pi(\tilde{x} + \tilde{h}) - \cos 2\pi\tilde{y}} + 2(1-2\nu)\pi\tilde{h} \\ &\times \frac{\sinh 2\pi(\tilde{x} - \tilde{h})}{\cosh 2\pi(\tilde{x} - \tilde{h}) - \cos 2\pi\tilde{y}} + \pi(\tilde{x} + \tilde{h}) \frac{\sinh 2\pi(\tilde{x} - \tilde{h})}{\cosh 2\pi(\tilde{x} - \tilde{h}) - \cos 2\pi\tilde{y}} - 4\pi^2\tilde{x}\tilde{h} \frac{1 - \cosh 2\pi(\tilde{x} - \tilde{h}) \cos 2\pi\tilde{y}}{[\cosh 2\pi(\tilde{x} - \tilde{h}) - \cos 2\pi\tilde{y}]^2} \end{aligned} \right\}, \tag{A11a}$$

$$u_y^{\Sigma b_y} = -\frac{b_y}{2\pi} \left\{ \tan^{-1} [\tanh \pi(\tilde{x} - \tilde{h}) \cot \pi\tilde{y}] - \tan^{-1} [\tanh \pi(\tilde{x} + \tilde{h}) \cot \pi\tilde{y}] \right\} + \frac{b_y}{4\pi(1-\nu)} \times \left\{ \begin{aligned} &\pi(\tilde{x} + \tilde{h}) \frac{\sin 2\pi\tilde{y}}{\cosh 2\pi(\tilde{x} + \tilde{h}) - \cos 2\pi\tilde{y}} + (3 - 4\nu)\pi\tilde{h} \frac{\sin 2\pi\tilde{y}}{\cosh 2\pi(\tilde{x} - \tilde{h}) - \cos 2\pi\tilde{y}} \\ &- \pi\tilde{x} \frac{\sin 2\pi\tilde{y}}{\cosh 2\pi(\tilde{x} - \tilde{h}) - \cos 2\pi\tilde{y}} - 4\pi^2\tilde{x}\tilde{h} \frac{\sinh 2\pi(\tilde{x} - \tilde{h}) \sin 2\pi\tilde{y}}{[\cosh 2\pi(\tilde{x} - \tilde{h}) - \cos 2\pi\tilde{y}]^2} \end{aligned} \right\}, \tag{A11b}$$

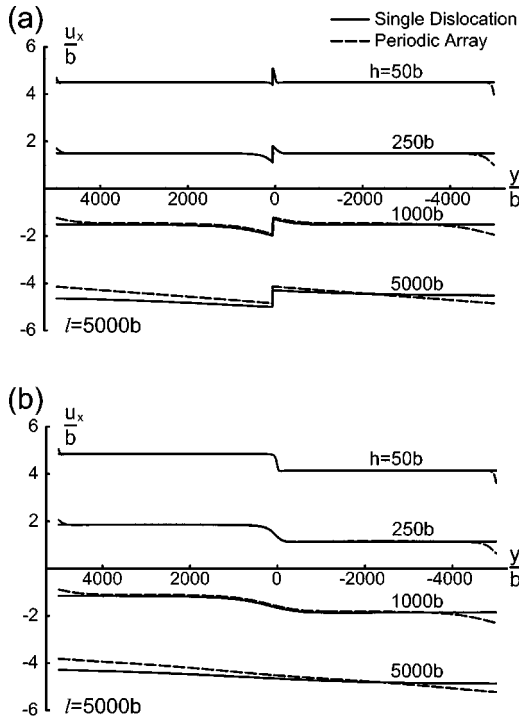


FIG. 11. Comparison of surface profiles for a single MD and for periodic array of MDs for SSO (a) and SSE (b) cases. MDs (single or in array) with the Burgers vector $\mathbf{b}=[(\sqrt{2}/\sqrt{3})\mathbf{e}_x+(1/\sqrt{3})\mathbf{e}_y]b$ are placed at distance h from the surface as indicated in the figure. For these plots Poisson's ratio $\nu=0.32$. The Cartesian coordinates correspond to those used in Fig. 10.

$$u_z^{\Sigma b_y} = 0. \quad (\text{A11c})$$

(iii) For an array of screw dislocations with $\mathbf{b}=b_z\mathbf{e}_z$:

$$u_x^{\Sigma b_z} = 0, \quad (\text{A12a})$$

$$u_y^{\Sigma b_z} = 0, \quad (\text{A12b})$$

$$u_z^{\Sigma b_z} = \frac{b_z}{2\pi} [\tan^{-1}[\tanh \pi(\tilde{x}-\tilde{h})\cot \pi\tilde{y}] - \tan^{-1}[\tanh \pi(\tilde{x}+\tilde{h})\cot \pi\tilde{y}]]. \quad (\text{A12c})$$

In Eqs. (A10)–(A12) we employed the normalized coordinates and film thickness: $\tilde{x}=x/l$, $\tilde{y}=y/l$, and $\tilde{h}=h/l$.

In Fig. 11 we compare the displacements of a single edge dislocation and a (infinite) periodic array of edge dislocations. The two sets of plots presented in Figs. 11(a) and 11(b) cover the two cases of the orientation of the slip step created when dislocations are introduced into the material, i.e., towards the free surface (SSO) and towards the bulk of the material (SSE), respectively.

The strains are defined by

$$\varepsilon_{ij} = \frac{1}{2} \left(\frac{\partial u_i}{\partial x_j} + \frac{\partial u_j}{\partial x_i} \right). \quad (\text{A13})$$

When applying Eq. (A13) to dislocation displacement fields, we must separate elastic and plastic deformations, as proposed by DeWit.²¹ The plastic contribution can be identified

by characteristic discontinuous step-like terms and can be omitted in the expression for elastic strains. Finally, elastic stresses are derived from Hooke's law

$$\sigma_{ij} = 2G \left(\varepsilon_{ij} + \frac{\nu}{1-2\nu} \varepsilon_{kk} \delta_{ij} \right), \quad (\text{A14})$$

where the shear modulus G and Poisson's ratio ν are the elastic constants for isotropic solid. For convenience, we also define $D = G/2\pi(1-\nu)$.

The components of the stress tensor for individual dislocations are as following.

(i) For an edge dislocations with $\mathbf{b}=b_x\mathbf{e}_x$:

$$\sigma_{xx}^{b_x} = Db_x \left\{ -\frac{y[3(x+h)^2+y^2]}{[(x+h)^2+y^2]^2} + \frac{y[3(x-h)^2+y^2]}{[(x-h)^2+y^2]^2} - 4xyh \frac{3(x-h)^2-y^2}{[(x-h)^2+y^2]^3} \right\}, \quad (\text{A15a})$$

$$\sigma_{yy}^{b_x} = Db_x \left\{ \frac{y[(x+h)^2-y^2]}{[(x+h)^2+y^2]^2} + \frac{y(7h^2-6hx-x^2+y^2)}{[(x-h)^2+y^2]^2} + 4xyh \frac{3(x-h)^2-y^2}{[(x-h)^2+y^2]^3} \right\}, \quad (\text{A15b})$$

$$\sigma_{xy}^{b_x} = Db_x \left\{ \frac{(x+h)[(x+h)^2-y^2]}{[(x+h)^2+y^2]^2} - \frac{(x+h)[(x-h)^2-y^2]}{[(x-h)^2+y^2]^2} + 4xh(x-h) \frac{(x-h)^2-3y^2}{[(x-h)^2+y^2]^3} \right\}, \quad (\text{A15c})$$

$$\sigma_{zz}^{b_x} = D\nu b_x \left\{ -\frac{2y}{(x+h)^2+y^2} + \frac{2y(5h^2-6hx+x^2+y^2)}{[(x-h)^2+y^2]^2} \right\}, \quad (\text{A15d})$$

$$\sigma_{xz}^{b_x} = \sigma_{yz}^{b_x} = 0. \quad (\text{A15e,f})$$

(ii) For an edge dislocation with $\mathbf{b}=-b_y\mathbf{e}_y$:

$$\sigma_{xx}^{b_y} = -Db_y \left\{ \frac{(x+h)[(x+h)^2-y^2]}{[(x+h)^2+y^2]^2} + \frac{(x-h)[(x-h)^2-y^2]}{[(x-h)^2+y^2]^2} + 2x \frac{h^4-2h^3x-x^4-6h^2y^2+y^4+2h(x^3+3xy^2)}{[(x-h)^2+y^2]^3} \right\}, \quad (\text{A16a})$$

$$\sigma_{yy}^{b_y} = -Db_y \left\{ \frac{(x+h)[(x+h)^2+3y^2]}{[(x+h)^2+y^2]^2} - \frac{h^3+h^2x-5h(x^2+y^2)+x(3x^2+y^2)}{[(x-h)^2+y^2]^2} - 2x \frac{h^4-2h^3x-x^4-6h^2y^2+y^4+2h(x^3+3xy^2)}{[(x-h)^2+y^2]^3} \right\}, \quad (\text{A16b})$$

$$\sigma_{xy}^{b_y} = -Db_y \left\{ \frac{y[(x+h)^2 - y^2]}{[(x+h)^2 + y^2]^2} + \frac{y(-h^2 - 2hx + 3x^2 + y^2)}{[(x-h)^2 + y^2]^2} - 4xy \frac{2h^3 - 3h^2x + x^3 - 2hy^2 + xy^2}{[(x-h)^2 + y^2]^3} \right\}, \quad (A16c)$$

$$\sigma_{zz}^{b_y} = -D\nu b_y \left\{ \frac{2(x+h)}{(x+h)^2 + y^2} - \frac{2[h^3 - h^2x + x(x^2 + y^2) - h(x^2 + 3y^2)]}{[(x-h)^2 + y^2]^2} \right\}; \quad (A16d)$$

$$\sigma_{xz}^{b_y} = \sigma_{yz}^{b_y} = 0. \quad (A16e,f)$$

(iii) For a screw dislocation with $\mathbf{b} = b_z \mathbf{e}_z$:

$$\sigma_{xx}^{b_z} = \sigma_{yy}^{b_z} = \sigma_{zz}^{b_z} = \sigma_{xy}^{b_z} = 0; \quad (A17a,b,c,d)$$

$$\sigma_{xz}^{b_z} = -\frac{Gb_z}{2\pi} \left\{ \frac{y}{(x+h)^2 + y^2} - \frac{y}{(x-h)^2 + y^2} \right\}; \quad (A17e)$$

$$\sigma_{yz}^{b_z} = \frac{Gb_z}{2\pi} \left\{ \frac{x+h}{(x+h)^2 + y^2} - \frac{x-h}{(x-h)^2 + y^2} \right\}. \quad (A17f)$$

The components of the stress tensor for an array of subsurface dislocations array stresses are as follows.

(i) For an array of edge dislocations with $\mathbf{b} = b_x \mathbf{e}_x$:

$$\sigma_{xx}^{\Sigma b_x} = D \frac{b_x}{l} \pi \left\{ \sin 2\pi\bar{y} \frac{\cos 2\pi\bar{y} - \cosh 2\pi(\bar{x} + \bar{h}) - 2\pi(\bar{x} + \bar{h}) \sinh 2\pi(\bar{x} + \bar{h})}{[\cosh 2\pi(\bar{x} + \bar{h}) - \cos 2\pi\bar{y}]^2} - \sin 2\pi\bar{y} \frac{\cos 2\pi\bar{y} - \cosh 2\pi(\bar{x} - \bar{h}) - 2\pi(\bar{x} - \bar{h}) \sinh 2\pi(\bar{x} - \bar{h})}{[\cosh 2\pi(\bar{x} - \bar{h}) - \cos 2\pi\bar{y}]^2} - 4\pi^2 \bar{x} \bar{h} \sin 2\pi\bar{y} \frac{-3 + \cosh 4\pi(\bar{x} - \bar{h}) + 2 \cosh 2\pi(\bar{x} - \bar{h}) \cos 2\pi\bar{y}}{[\cosh 2\pi(\bar{x} - \bar{h}) - \cos 2\pi\bar{y}]^3} \right\}, \quad (A18a)$$

$$\sigma_{yy}^{\Sigma b_x} = D \frac{b_x}{l} \pi \left\{ \sin 2\pi\bar{y} \frac{\cos 2\pi\bar{y} - \cosh 2\pi(\bar{x} + \bar{h}) + 2\pi(\bar{x} + \bar{h}) \sinh 2\pi(\bar{x} + \bar{h})}{[\cosh 2\pi(\bar{x} + \bar{h}) - \cos 2\pi\bar{y}]^2} - \sin 2\pi\bar{y} \frac{\cos 2\pi\bar{y} - \cosh 2\pi(\bar{x} - \bar{h}) + 2\pi(\bar{x} - \bar{h}) \sinh 2\pi(\bar{x} - \bar{h})}{[\cosh 2\pi(\bar{x} - \bar{h}) - \cos 2\pi\bar{y}]^2} + 4\pi^2 \bar{x} \bar{h} \sin 2\pi\bar{y} \frac{-3 + \cosh 4\pi(\bar{x} - \bar{h}) + 2 \cosh 2\pi(\bar{x} - \bar{h}) \cos 2\pi\bar{y}}{[\cosh 2\pi(\bar{x} - \bar{h}) - \cos 2\pi\bar{y}]^3} \right\}, \quad (A18b)$$

$$\sigma_{xy}^{\Sigma b_x} = D \frac{b_x}{l} \pi \left\{ 2\pi(\bar{x} + \bar{h}) \frac{\cos 2\pi\bar{y} \cosh 2\pi(\bar{x} + \bar{h}) - 1}{[\cosh 2\pi(\bar{x} + \bar{h}) - \cos 2\pi\bar{y}]^2} - 2\pi(\bar{x} + \bar{h}) \frac{\cos 2\pi\bar{y} \cosh 2\pi(\bar{x} - \bar{h}) - 1}{[\cosh 2\pi(\bar{x} - \bar{h}) - \cos 2\pi\bar{y}]^2} + 4\pi^2 \bar{x} \bar{h} \frac{[-3 + \cos 4\pi\bar{y} + 2 \cos 2\pi\bar{y} \cosh 2\pi(\bar{x} - \bar{h})] \sinh 2\pi(\bar{x} - \bar{h})}{[\cosh 2\pi(\bar{x} - \bar{h}) - \cos 2\pi\bar{y}]^3} \right\}, \quad (A18c)$$

$$\sigma_{zz}^{\Sigma b_x} = -D\nu \frac{b_x}{l} \pi \left\{ \frac{2 \sin 2\pi\bar{y}}{\cosh 2\pi(\bar{x} + \bar{h}) - \cos 2\pi\bar{y}} + 2 \sin 2\pi\bar{y} \frac{\cos 2\pi\bar{y} - \cosh 2\pi(\bar{x} - \bar{h}) + 4\pi\bar{h} \sinh 2\pi(\bar{x} - \bar{h})}{[\cosh 2\pi(\bar{x} - \bar{h}) - \cos 2\pi\bar{y}]^2} \right\}; \quad (A18d)$$

$$\sigma_{xz}^{\Sigma b_x} = \sigma_{yz}^{\Sigma b_x} = 0. \quad (A18e,f)$$

(ii) For an array of edge dislocations with $\mathbf{b} = -b_y \mathbf{e}_y$:

$$\sigma_{xx}^{\Sigma b_y} = D \frac{b_y}{l} \pi \left\{ -2\pi(\tilde{x} + \tilde{h}) \frac{\cosh 2\pi(\tilde{x} + \tilde{h})\cos 2\pi\tilde{y} - 1}{[\cosh 2\pi(\tilde{x} + \tilde{h}) - \cos 2\pi\tilde{y}]^2} - 2\pi(\tilde{x} - \tilde{h}) \frac{\cosh 2\pi(\tilde{x} - \tilde{h})\cos 2\pi\tilde{y} - 1}{[\cosh 2\pi(\tilde{x} - \tilde{h}) - \cos 2\pi\tilde{y}]^2} \right. \\ \left. + 2\pi\tilde{x} \frac{3\cos 2\pi\tilde{y} - \cosh 2\pi(\tilde{x} - \tilde{h})(3 + \cos 4\pi\tilde{y})}{[\cosh 2\pi(\tilde{x} - \tilde{h}) - \cos 2\pi\tilde{y}]^3} \right. \\ \left. + 2\pi\tilde{x} \frac{[\cosh 4\pi(\tilde{x} - \tilde{h}) + 2\pi\tilde{h} \sinh 4\pi(\tilde{x} - \tilde{h})]\cos 2\pi\tilde{y} - 2\pi\tilde{h} \sinh 2\pi(\tilde{x} - \tilde{h})(3 - \cos 4\pi\tilde{y})}{[\cosh 2\pi(\tilde{x} - \tilde{h}) - \cos 2\pi\tilde{y}]^3} \right\}, \tag{A19a}$$

$$\sigma_{yy}^{\Sigma b_y} = D \frac{b_y}{l} \pi \left\{ \frac{2\pi(\tilde{x} + \tilde{h})[\cosh 2\pi(\tilde{x} + \tilde{h})\cos 2\pi\tilde{y} - 1] + 2\sinh 2\pi(\tilde{x} + \tilde{h})\cos 2\pi\tilde{y} - \sinh 4\pi(\tilde{x} + \tilde{h})}{[\cosh 2\pi(\tilde{x} + \tilde{h}) - \cos 2\pi\tilde{y}]^2} \right. \\ \left. + \frac{2\pi(\tilde{x} + 3\tilde{h})[\cosh 2\pi(\tilde{x} - \tilde{h})\cos 2\pi\tilde{y} - 1] - 2\sinh 2\pi(\tilde{x} - \tilde{h})\cos 2\pi\tilde{y} + \sinh 4\pi(\tilde{x} - \tilde{h})}{[\cosh 2\pi(\tilde{x} - \tilde{h}) - \cos 2\pi\tilde{y}]^2} \right. \\ \left. - 2\pi\tilde{x} \frac{3\cos 2\pi\tilde{y} - \cosh 2\pi(\tilde{x} - \tilde{h})(3 + \cos 4\pi\tilde{y})}{[\cosh 2\pi(\tilde{x} - \tilde{h}) - \cos 2\pi\tilde{y}]^3} \right. \\ \left. - 2\pi\tilde{x} \frac{[\cosh 4\pi(\tilde{x} - \tilde{h}) + 2\pi\tilde{h} \sinh 4\pi(\tilde{x} - \tilde{h})]\cos 2\pi\tilde{y} - 2\pi\tilde{h} \sinh 2\pi(\tilde{x} - \tilde{h})(3 - \cos 4\pi\tilde{y})}{[\cosh 2\pi(\tilde{x} - \tilde{h}) - \cos 2\pi\tilde{y}]^3} \right\}, \tag{A19b}$$

$$\sigma_{xy}^{\Sigma b_y} = D \frac{b_y}{l} \pi \left\{ -\sin 2\pi\tilde{y} \frac{2\pi(\tilde{x} + \tilde{h})\sinh 2\pi(\tilde{x} + \tilde{h}) + \cos 2\pi\tilde{y} - \cosh 2\pi(\tilde{x} + \tilde{h})}{[\cosh 2\pi(\tilde{x} + \tilde{h}) - \cos 2\pi\tilde{y}]^2} \right. \\ \left. + \sin 2\pi\tilde{y} \frac{-2\pi(\tilde{x} + \tilde{h})\sinh 2\pi(\tilde{x} - \tilde{h}) + \cos 2\pi\tilde{y} - \cosh 2\pi(\tilde{x} - \tilde{h})}{[\cosh 2\pi(\tilde{x} - \tilde{h}) - \cos 2\pi\tilde{y}]^2} + 4\pi\tilde{x} \sin 2\pi\tilde{y} \right. \\ \left. \times \frac{2\pi\tilde{h} \cosh 2\pi(\tilde{x} - \tilde{h})\cos 2\pi\tilde{y} - 3\pi\tilde{h} + \pi\tilde{h} \cosh 4\pi(\tilde{x} - \tilde{h}) + \sinh 2\pi(\tilde{x} - \tilde{h})[\cosh 2\pi(\tilde{x} - \tilde{h}) - \cos 2\pi\tilde{y}]}{[\cosh 2\pi(\tilde{x} - \tilde{h}) - \cos 2\pi\tilde{y}]^3} \right\}, \tag{A19c}$$

$$\sigma_{zz}^{\Sigma b_y} = D\nu \frac{b_y}{l} \pi \left\{ \frac{-2\sinh 2\pi(\tilde{x} + \tilde{h})}{[\cosh 2\pi(\tilde{x} + \tilde{h}) - \cos 2\pi\tilde{y}]} \right. \\ \left. + \frac{-8\pi\tilde{h} + 8\pi\tilde{h} \cosh 2\pi(\tilde{x} - \tilde{h})\cos 2\pi\tilde{y} - 2\sinh 2\pi(\tilde{x} - \tilde{h})\cos 2\pi\tilde{y} + \sinh 4\pi(\tilde{x} - \tilde{h})}{[\cosh 2\pi(\tilde{x} - \tilde{h}) - \cos 2\pi\tilde{y}]^2} \right\}, \tag{A19d}$$

$$\sigma_{xz}^{\Sigma b_y} = \sigma_{yz}^{\Sigma b_y} = 0. \tag{A19e,f}$$

(iii) For an array of screw dislocations with $\mathbf{b} = b_z \mathbf{e}_z$:

$$\sigma_{xx}^{\Sigma b_z} = \sigma_{yy}^{\Sigma b_z} = \sigma_{zz}^{\Sigma b_z} = \sigma_{xy}^{\Sigma b_z} = 0, \tag{A20a,b,c,d}$$

$$\sigma_{xz}^{\Sigma b_z} = G \frac{b_z}{2l} \left[-\frac{\sin 2\pi\tilde{y}}{\cosh 2\pi(\tilde{x} + \tilde{h}) - \cos 2\pi\tilde{y}} + \frac{\sin 2\pi\tilde{y}}{\cosh 2\pi(\tilde{x} - \tilde{h}) - \cos 2\pi\tilde{y}} \right], \tag{A20e}$$

$$\sigma_{yz}^{\Sigma b_z} = G \frac{b_z}{2l} \left[\frac{\sinh 2\pi(\tilde{x} + \tilde{h})}{\cosh 2\pi(\tilde{x} + \tilde{h}) - \cos 2\pi\tilde{y}} - \frac{\sinh 2\pi(\tilde{x} - \tilde{h})}{\cosh 2\pi(\tilde{x} - \tilde{h}) - \cos 2\pi\tilde{y}} \right]. \tag{A20f}$$

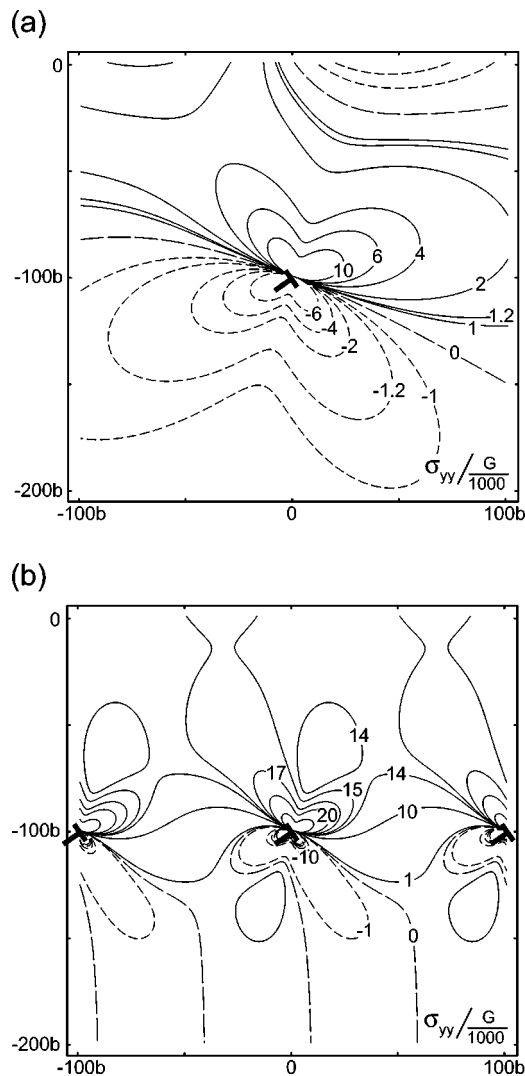


FIG. 12. Examples of stress distribution due to MDs. Contour plots of MD stresses σ_{yy} for an individual dislocation (a) and periodic dislocation array (b). For these plots dislocations with Burgers vector $\mathbf{b}=[(\sqrt{2}/\sqrt{3})\mathbf{e}_x + (1/\sqrt{3})\mathbf{e}_y]b$ were at the distance $h=100b$ from the free surface, periodicity in the array was $l=100b$, Poisson's ratio $\nu=0.32$. Stresses are in the units of $10^{-3} G$. The Cartesian coordinates correspond to those used in Fig. 10.

The stresses in Eqs. (A15)–(A20), satisfy the boundary and equilibrium conditions given by Eqs. (A1).

The stresses for the periodic dislocation array [Eqs. (A18)–(A20)] can be transformed back to the solution for a single dislocation placed at the distance h from the free surface [Eqs. (A15)–(A17)] by solving for the limit as $l \rightarrow \infty$. The agreement with known results for a single dislocation provides a good check on the Eqs. (A16)–(A20). Figure 12 shows the comparison between the tangential component of the stress σ_{yy} arising from a dislocation array with those from a single edge dislocation.

We note here that the derived displacements and stress

fields for periodic subsurface dislocations could be obtained in a different way from summation of Fourier series expressions given in Ref. 22 for dislocation arrays in two dissimilar elastic phase material. Using this technique, the formulas for the stresses of periodic subsurface edge dislocation arrays [which are equivalent to Eqs. (A18) and (A19)] were obtained in Ref. 23. The stresses for screw dislocation arrays were already used in Ref. 24. Finally, the normal component of the displacement field originating from subsurface edge dislocation arrays was utilized in Ref. 25 when studying the surface profile of InAs/GaAs (110) films.

In our modeling of crosshatch surface morphology, we use the displacements and stresses at the film surface, which can be easily extracted from the general solutions by putting $x=0$. In addition, to make the presentation of the modeling results more convenient, the stress and displacements equations are transformed so that sample surface is along the x axis, the sample surface normal is along the y axis, and the dislocation is at $(0, -h)$. This orientation is used for all the figures in the main text.

- ¹A. M. Andrews, A. E. Romanov, J. S. Speck, M. Bobeth, and W. Pompe, *Appl. Phys. Lett.* **77**, 3740 (2000).
- ²A. M. Andrews, J. S. Speck, A. E. Romanov, M. Bobeth, and W. Pompe, *J. Appl. Phys.* **91**, 1933 (2002).
- ³H. Norenberg, L. Daweritz, P. Schutzendube, and K. Ploog, *J. Appl. Phys.* **81**, 2611 (1997).
- ⁴T. Ogura, D. Kishimoto, and T. Nishinaga, *J. Cryst. Growth* **226**, 179 (2001).
- ⁵A. Kley, P. Ruggerone, and M. Scheffler, *Phys. Rev. Lett.* **79**, 5278 (1997).
- ⁶J. W. Matthews, in *Dislocations in Solids*, edited by F. R. N. Nabarro (North-Holland, Amsterdam, 1979), Vol. 2, p. 461.
- ⁷E. A. Fitzgerald, *Mater. Sci. Rep.* **7**, 87 (1991).
- ⁸L. B. Freund, *MRS Bull.* **17**, 52 (1992).
- ⁹R. Beanland, D. J. Dunstan, and P. J. Goodhew, *Adv. Phys.* **45**, 87 (1996).
- ¹⁰J. S. Speck, M. A. Brewer, G. E. Beltz, A. E. Romanov, and W. Pompe, *J. Appl. Phys.* **80**, 3808 (1996).
- ¹¹J. W. Matthews and A. E. Blakeslee, *J. Cryst. Growth* **27**, 118 (1974).
- ¹²J. Y. Tsao, *Materials Fundamentals of Molecular Beam Epitaxy* (Academic, New York, 1993).
- ¹³A. Krost, G. Bauer, J. Woitok, in *Optical Characterization of Epitaxial Semiconductor Layers* edited by G. Bauer and W. Richter (Springer, New York, 1996), Chap. 6.
- ¹⁴K. Cholevas, N. Liosatos, A. E. Romanov, M. Zaiser, and E. C. Aifantis, *Phys. Status Solidi B* **209**, 295 (1998).
- ¹⁵U. Jain, S. C. Jain, A. Atkinson, J. Nijs, R. P. Mertens, and R. Van Overstraeten, *J. Appl. Phys.* **73**, 1773 (1993).
- ¹⁶A. K. Head, *Proc. Phys. Soc. London, Sect. B* **66**, 793 (1953).
- ¹⁷J. D. Eshelby, in *Dislocations in Solids*, edited by F. R. N. Nabarro (North-Holland, Amsterdam, 1979), Vol. 1, p. 167.
- ¹⁸J. P. Hirth and J. Lothe, *Theory of Dislocations* (Wiley, New York, 1982).
- ¹⁹M. Dynna, J. L. Vassent, A. Marty, and B. Gilles, *J. Appl. Phys.* **80**, 2650 (1996).
- ²⁰K. Jagannadham and M. J. Marcinkowski, *J. Mater. Sci.* **15**, 709 (1980).
- ²¹R. De Wit, *J. Res. Natl. Bur. Stand.* **77A**, 607 (1973).
- ²²R. Bonnet and J. L. Verger-Gaugry, *Philos. Mag. A* **66**, 849 (1992).
- ²³A. Bourret, *Surf. Sci.* **432**, 37 (1999).
- ²⁴A. E. Romanov, P. M. Petroff, and J. S. Speck, *Appl. Phys. Lett.* **74**, 2280 (1999).
- ²⁵J. G. Belk, D. W. Pashley, B. A. Joyce, and T. S. Jones, *Phys. Rev. B* **58**, 16194 (1998).